

## Phase field modeling of fracture and crack growth

A. Staroselsky<sup>a,\*</sup>, R. Acharya<sup>a</sup>, B. Cassenti<sup>b</sup>



<sup>a</sup>United Technologies Research Center, East Hartford, CT, United States

<sup>b</sup>University of Connecticut, Storrs, CT, United States

### ARTICLE INFO

**Keywords:**

Phase field  
Crack propagation  
Crack arrest  
Crack tip velocity

### ABSTRACT

Predicting crack growth in structural components is a computationally intensive process. Phase field models of crack growth reduce the computational complications associated with singularities, and allow finite element predictions of crack propagation without remeshing. A novel approach to derive governing equations based on a Lagrangian density is proposed and the phase evolution is shown to be governed by a diffusion type equation with a source term. We correlate the phase to the micromechanical response. The model was incorporated in a finite element code and used to predict crack growth phenomena including (1) values of critical stress, (2) crack path, and (3) crack bifurcation. It was shown that the values of the critical stresses can be accurately estimated by the change in the phase field crack tip velocity or by the use of energy contour integral. The phase field crack analysis is compared against LEFM results.

### 1. Introduction

For many engineering applications, such as the life prediction of blades in jet engines, crack propagation is extremely dangerous and may result in catastrophic failures. On the other hand if the crack has been initiated in a high stress concentration zone then, although failure may be likely, the crack could stop and its propagation is arrested as it grows out of the high stress concentration zone. The concept of damage tolerant design postulates that a part always contains some microcracks. The part should remain in operation until the crack growth rate, and crack sizes are above some critical values. It allows for significant reductions in maintenance spending. To achieve all these economic benefits from appropriate maintenance resources, an accurate estimation of failure time and reliability assessment is necessary. Most of the currently used engineering tools for structural life prediction estimate fatigue life or crack propagation based on the worst local conditions, hence ignoring the crack growth and possible arrest. Such an analysis is performed by calculating either stress intensity factors (SIF) or energy release rate ( $J$ -integral). Both of these are crack-tip parameters that characterize the asymptotic field of crack singularities in elastic or elastic-plastic materials, and an enormous amount of research has been conducted on that subject. Hence, computation of crack propagation requires sequential application of crack tip analyses for evolving crack geometry and loading conditions. This procedure is defined as computational fracture mechanics and even with significant advancement; it remains a challenging problem.

Predicting the life and failure of structural parts with complex material morphology and geometry is a complicated task. Usually, numerical approaches such as the finite element method (FEM) [1,2], boundary elements (BEM) [3], or their hybrids [4,5] are used to predict crack path and critical values of applied loads. It is important, that in general formulations of linear elastic fracture mechanics (LEFM) and elastic-plastic fracture mechanics (EPFM) the crack paths and bifurcation prediction is usually limited to isotropic materials. For example, the current inelastic material models have proven difficult to use when cracks are present in Single-crystal

\* Corresponding author.

E-mail address: [starosav@utrc.utc.com](mailto:starosav@utrc.utc.com) (A. Staroselsky).

(SX) components [6], which is crucial for the reliability analysis of SX turbine blades. SX nickel-base superalloys, exhibit both elastic and plastic anisotropy and nonlinear characteristics, where inelastic deformation is the primary damage-inducing mechanism. Therefore, fracture prediction of these materials is complicated. It has been shown [7–9], that the anisotropy linked to the crystallographic structure, has a considerable impact on crack propagation. It is important, that in general formulations, BEM and FEM/BEM methods are typically applicable to linear fracture mechanics problems and cannot predict the crack paths and bifurcation in those materials with specific critical planes for crack growth. The models are numerically difficult to implement and the inclusion of cracks and other singularities makes them even more difficult [10,11]. Fracture mechanics numerical simulations require re-meshing in order to handle crack propagation resulting in lengthy computational times. Yet these methods do not accurately predict the instabilities at the crack tips, or at the kinks, nor do they accurately predict the crack tip velocity. Using current methods of fracture mechanics, it has been extremely difficult to handle the instabilities of rapid dynamic crack growth [12–14] including crack kinking or branching [15–17]. All this motivates researchers to consider alternative approaches for crack propagation that complement existing computational methods. We will not consider these effects in detail, but the method we use to derive the governing equations may make it possible to advance in these areas.

Another important point that needs to be noted is that LEFM, and even EPFM models ignore a number of actual physical phenomena such as material evolution and damage propagation. These classical approaches are oversimplified. Cracking and failure of structural parts often takes place after significant degradation of the material microstructure in the crack process zone. The introduction of approximations such as the field variables (or tensors in the case of anisotropic materials) can be quite valuable. For example, a variable gradually changing from unity, representing intact material, to zero, corresponding to fully damaged state can be used. Such a variable can be fully coupled with the displacement field. Damage mechanics uses this approach by defining a damage parameter. It is widely used in analysis of creep and/or plasticity driven material property evolution and rupture prediction [17–21]. The application of damage mechanics to the analysis of high stress concentrations at the crack tip leads to the use of non-local approaches where the gradient of the damage parameter is included in the governing equation. Such a model reveals the strong effects of gradients on crack propagation laws and the value of the potential energy [22].

Natural extensions of non-local methods include attempts to represent crack growth by phase field equations, see for example [23–25]. Consider the case where the state of the entire microstructure is represented continuously by a single variable known as the order parameter or phase indicator,  $\phi$ , where  $0 \leq \phi \leq 1$ . Pristine material is represented by a constant value of phase indicator, taken to be equal to 1. The interior of a crack is represented by the value  $\phi = 0$ , while the interface corresponds to the domain where phase indicator changes (i.e.,  $0 < \phi < 1$ ). It can be seen as a gradual change of damage in the process zone decreasing away from the crack tips. Thus, this mathematical formulation assumes a diffused interface or, in other words, it assumes that interfaces have finite thickness where physical quantities vary from their bulk values [26]. The energy term describing the interface is a function of  $\nabla\phi$ . The total free energy is then described in terms of the order parameter,  $\phi$ , and its gradients. Phase field (or diffuse) methods are based on minimization of the system free energy of the volume including gradients of the thermodynamic variables accounting for non-local effects. The rate at which the microstructure evolves, or the rate the crack propagates with time is based on irreversible thermodynamics and depends on how energy density varies with  $\phi$  and its gradient. All state variables and parameters in this approach depend on the phase indicator, and subsequently, automatically change with the evolution of the structure. Thus, with a single functional to describe the evolution of the phase field, coupled with material constitutive equations one can describe the cracking, irrespective of the number and shape of cracks in the part. Thus, in phase field formulations, failure is treated as a phase transition problem, the locations of the crack tips no longer need to be tracked but can be calculated from the evolution of field parameters. Numerically, it means that there is no longer any need for special mesh elements around crack tip singularities. This provides significant benefits for finite element method implementation, since it eliminates the extremely expensive numerical re-meshing operation. However, it may cause crack widening and lateral growth during crack propagation [27,28]. Levitas et. al also discussed consistent and scale dependent phase field approach for crack propagation considering surface stresses [29].

However, the formulation of the energy density functional is to some extent empirical. There is still no clear and accurate mechanistic derivation for phase field fracture models based on micromechanics. An understanding of the model's physical basis and an accurate definition of the physical properties used in the energy density potential is crucial for correct problem formulation. Hence the first goal of this work is to develop a consistent phase field formulation for predicting crack propagation based on a variational approach bridging the gap between mesoscale and continuum scales [30]. This would allow a better understanding of the fundamental characteristics of the formulation and its connection with material structure.

It is important to be aware that when using phase field equations for crack propagation analysis we can substitute classical elliptic equations in steady state cases or hyperbolic equations in dynamic problems with the parabolic equations for the phase field. The phase has a square root singularity around plane cuts, which in turn allows solutions to be in a good accord with classical solid mechanics results. Such an equation does not generally have steady state solutions, meaning that cracks always propagate under any loading condition; however, depending on loading values it may be extremely slow or extremely fast. Hence, phase field models routinely predict crack path but it is difficult to resolve the critical stress. In this paper, we attempt to correlate crack critical stress values with the derived crack tip propagation velocity from phase field solutions.

The plan of the paper is as follows: the next section outlines the derivation of the phase-field type model for crack problems from basic mechanical principles and connects it to the materials mesoscale parameters. Section 3 defines the model parameters and methods to guarantee process irreversibility, i.e. methods to exclude crack healing under compression as possible model outcomes. Results of numerical analyses are given in Section 4 where phase-field model predictions are compared against fracture mechanics solutions for particular material parameters. The applicability of the several local criteria for determination of critical stresses in phase-field formulation is also presented. We close the paper with some additional discussion and concluding remarks.

## 2. Phase field crack propagation

### 2.1. Review of minimum action principle

Equations of motion are readily generated for conservative systems using the Lagrangian,  $L$ , formed by subtracting the potential energy,  $V$ , from the kinetic energy,  $T$ . The action,  $S$ , can then be created by integrating the Lagrangian over time. Minimizing the action between times  $t_1$  and  $t_2$  yields the governing equations of motion. For a continuous system, a Lagrangian density can be used and when integrated over the volume will yield the action. It is important to note that when the action is minimized, it will result in a second derivative of the dependent variables with respect to time but the desired diffusion equation contains only the first derivative with respect to time. This apparent contradiction is removed by considering the random motion of molecules in a material [30].

A Lagrangian readily yields the wave equation for continuous systems but developing a formulation that produces a diffusion equation is more difficult. Ref. [30] has solved the problem by considering the random motion present in diffusion processes. Following [30], the kinetic energy consists of two parts: (1) a uniform or global component, and (2) a random or local component. For an isotropic material the random component has a velocity that is assumed to be isotropic so that its integral (average) over the  $4\pi$  spherical angle vanishes.

The kinetic energy density,  $T$ , can be written as [30]

$$T = \frac{1}{2}\rho\dot{u}_i\dot{u}_i + \frac{1}{2}\rho\tilde{u}^2 \quad (1)$$

where,  $\rho$  is the density,  $\dot{u}_i$  is the uniform velocity,  $\tilde{u}$  is the random velocity. Note that a dot above a variable represents the partial derivative with respect to time and a repeated index over the spatial dimensions is summed.

For the total Lagrangian density we need to subtract the potential energy density from the kinetic energy density. In a solid, the potential energy density will consist of several components. The elastic energy will follow from the uniform displacements,  $u_i$ , Body forces,  $F_i$ , will contribute to the potential energy and there is energy from the amplitude of the random displacement,  $\tilde{u}$ . The total potential energy density can be written as:

$$V = \frac{1}{2}\sigma_{ij}\varepsilon_{ij} + F_i u_i + \frac{1}{2}K'\tilde{u}_{,i}\tilde{u}_{,i} \quad (2)$$

where  $K'$  is a material parameter,

$$\varepsilon_{ij} = \frac{1}{2}(u_{i,j} + u_{j,i}) \quad (3)$$

is the strain, and the stress, for an isotropic thermo-elastic material, is

$$\sigma_{ij} = 2\mu\varepsilon_{ij} + \lambda\varepsilon_{kk}\delta_{ij} - \alpha(2\mu + 3\lambda)(T - T_R)\delta_{ij} \quad (4)$$

where  $\mu$ ,  $\lambda$  are the Lame' elastic constants,  $\alpha$  is the thermal expansion coefficient,  $T$  is the temperature,  $T_R$  is the reference temperature, and a comma represents the partial derivative with respect to the spatial coordinate. It is important to recognize that the random velocity and displacement are directly related to the temperature.

The total Lagrangian density is

$$L = T - V = \frac{1}{2}\rho\dot{u}_i\dot{u}_i + \frac{1}{2}\rho\tilde{u}^2 - \frac{1}{2}\sigma_{ij}\varepsilon_{ij} - F_i u_i - \frac{1}{2}K'\tilde{u}_{,i}\tilde{u}_{,i}. \quad (5)$$

The degrees of freedom are  $u_i, \tilde{u}$ , and  $\tilde{u}'$ . The degrees of freedom  $\tilde{u}$ , and  $\tilde{u}'$  are related through the vibrations of the molecules in the solid and which are related to the temperature. Also note that  $\sigma_{ij}$  includes the temperature through the thermal strains in addition to the temperature dependence of the moduli, the thermal expansion coefficient, the density and parameter  $K'$ .

The action is found by integrating the Lagrangian over time from times  $t_1$  to  $t_2$  and over the volume  $\mathcal{V}$ , that is

$$S = \int_{t_1}^{t_2} \int_{\mathcal{V}} L d\mathcal{V} dt. \quad (6)$$

The variation of the action is zero

$$\delta S = 0 \quad (7)$$

or

$$\frac{\partial S}{\partial u_i} \delta u_i + \frac{\partial S}{\partial \tilde{u}} \delta \tilde{u} + \frac{\partial S}{\partial \tilde{u}'} \delta \tilde{u}' + \frac{\partial S}{\partial T} \delta T = 0. \quad (8)$$

Using [30] the random displacements and random velocities can be related through

$$\tilde{u} = \frac{1}{\Omega_0} \tilde{u}', \quad (9)$$

where  $\Omega_0$  is the primary frequency of vibration of the molecules and is related to the temperature,

$$\tilde{u} = \sqrt{\frac{fkT}{m}} = \sqrt{4C_p T}, \quad (10)$$

where  $f$  is the number of active degrees of freedom,  $k$  is Boltzmann's constant,  $m$  is the molecular mass, and  $C_p$  is the specific heat. The parameter  $K'$  is related to the thermal conductivity,  $K$ ,

$$K = 4C_p K' / \Omega_0. \quad (11)$$

For non-cryogenic temperatures the temperature dependence, from [31,32], is

$$K = K_0 \frac{\Theta_D}{T}, \quad (12)$$

where  $K_0$  is the reference conductivity at the Debye temperature  $\Theta_D$ .

Following standard mechanics, after minimizing the action, the governing equations are

$$\rho \ddot{u}_i = \sigma_{ij,j} + F_i, \quad (13a)$$

and,

$$\zeta \frac{\partial \dot{u}}{\partial t} = (K' \tilde{u}_{,i})_{,i} - \frac{1}{2} \frac{\partial K'}{\partial \tilde{u}} \tilde{u}_{,i} \tilde{u}_{,i} + \frac{\partial \sigma_{ij}}{\partial (\partial \tilde{u} / \partial t)} \dot{\varepsilon}_{ij}, \quad (13b)$$

where it is assumed that  $\partial \tilde{u} / \partial t = \dot{\tilde{u}} / \zeta$  relates the random velocities to the rate of change of the random displacements. In Appendix A we show that Eq. (13b) can be readily reduced to the Fourier heat conduction equation.

Non-conservative forces must be added to the right hand side of the conservation of momentum. The virtual work done,  $\delta W^{nc}$ , by the non-conservative forces is found by multiplying the forces by the virtual displacements of the degrees of freedom,  $\delta u_i$ . As an example consider the non-conservative stresses,  $\sigma_{ij}^{nc}$  due to Newtonian viscosity

$$\sigma_{ij}^{nc} = \eta \left( \dot{\varepsilon}_{ij} - \frac{1}{3} \dot{\varepsilon}_{kk} \delta_{ij} \right) \quad (14)$$

where  $\eta$  is the viscosity coefficient. The virtual work due to  $\sigma_{ij}^{nc}$  is

$$\delta W^{nc} = \int_V \sigma_{ij}^{nc} \delta \varepsilon_{ij} dV = \int_V \sigma_{ij}^{nc} \delta u_{i,j} dV = - \int_V \sigma_{ij,i}^{nc} \delta u_i dV \quad (15)$$

Hence the corresponding non-conservative force is  $-\sigma_{ij,i}^{nc}$ . Eq. (13a) remains the same while Eq. (4) for the stresses becomes

$$\sigma_{ij} = 2\mu \varepsilon_{ij} + \lambda \varepsilon_{kk} \delta_{ij} - \alpha(2\mu + 3\lambda)(T - T_R) \delta_{ij} + \eta \left( \dot{\varepsilon}_{ij} - \frac{1}{3} \dot{\varepsilon}_{kk} \delta_{ij} \right). \quad (16)$$

## 2.2. Addition of phase equation

Phase field representations of materials have been an active field of investigation over the last decade and have been found to be especially useful for predicting the propagation of cracks. In crack propagation simulations the phase,  $\phi$ , is one for pristine material and zero for failed materials. The evolution of the phase is represented by a diffusion equation. Hence, it will have a representative random displacement,  $\tilde{U}$ , and a representative random velocity,  $\dot{\tilde{U}}$ , and can be developed in a manner similar to the thermal diffusion equation.

The Lagrangian now becomes

$$L = \frac{1}{2} \rho \ddot{u}_i \dot{u}_i + \frac{1}{2} \rho \dot{\tilde{U}}^2 + \frac{1}{2} \rho \dot{U}^2 - \frac{1}{2} \sigma_{ij} \varepsilon_{ij} - F_i u_i - \frac{1}{2} K' \tilde{u}_{,i} \tilde{u}_{,i} - V_{DW}(\phi) - \frac{1}{2} \kappa'_{ij} \tilde{U}_{,i} \tilde{U}_{,j} \quad (17)$$

where  $\kappa'_{ij}$  is an anisotropic material parameter and  $V_{DW}(\phi)$  is a double well potential with minimums at  $\phi$  equal to zero and one.

The random phase displacements and velocities can be taken as related by an equation similar to Eq. (9)

$$\dot{\tilde{U}} = \Omega_1 \tilde{U}, \quad (18)$$

where  $\Omega_1$  is a characteristic frequency, similar to  $\Omega_0$  in Eq. (9), that represents the motion of the molecules while changing phase.

The variation becomes

$$\delta L = \rho \dot{\tilde{U}} \delta \tilde{U} - \frac{1}{2} \frac{\partial \sigma_{ij}}{\partial \phi} \varepsilon_{ij} \frac{d\phi}{d\tilde{U}} \delta \tilde{U} - \frac{dV_{DW}}{d\phi} \frac{d\phi}{d\tilde{U}} \delta \tilde{U} - \kappa' \tilde{U}_{,i} \delta \tilde{U}_{,i} - \frac{\partial \kappa'}{\partial \phi} \frac{d\phi}{d\tilde{U}} \tilde{U}_{,i} \delta \tilde{U} = 0. \quad (19)$$

Integrating the first and fourth terms by parts and taking integrand equal to zero

$$\delta L = - \frac{\partial(\rho \dot{\tilde{U}})}{\partial t} \delta \tilde{U} - \frac{1}{2} \frac{\partial \sigma_{ij}}{\partial \phi} \varepsilon_{ij} \frac{d\phi}{d\tilde{U}} \delta \tilde{U} - \frac{dV_{DW}}{d\phi} \phi \frac{d\phi}{d\tilde{U}} \delta \tilde{U} + (\kappa' \tilde{U}_{,i})_{,i} \delta \tilde{U} - \frac{\partial \kappa'}{\partial \phi} \frac{d\phi}{d\tilde{U}} \tilde{U}_{,i} \tilde{U}_{,i} \delta \tilde{U} = 0. \quad (20)$$

Since  $\delta \tilde{U}$  is arbitrary

$$-\frac{\partial(\rho\tilde{U})}{\partial t} - \frac{1}{2}\frac{\partial\sigma_{ij}}{\partial\phi}\varepsilon_{ij}\frac{d\phi}{d\tilde{U}} - \frac{dV_{DW}}{d\phi}\frac{d\phi}{d\tilde{U}} + (\kappa'\tilde{U}_{,i})_{,i} - \frac{\partial\kappa'}{\partial\phi}\frac{d\phi}{d\tilde{U}}\tilde{U}_{,i}\tilde{U}_{,i} = 0. \quad (21)$$

Setting  $\dot{\tilde{U}} = \Omega_1\tilde{U}$  and assuming  $\rho$  and  $\Omega_1$  are constant, then

$$\rho\Omega_1^2\frac{\partial\tilde{U}}{\partial t} = (\kappa'\tilde{U}_{,i})_{,i} - \frac{1}{2}\frac{\partial\sigma_{ij}}{\partial\phi}\varepsilon_{ij}\frac{\partial\phi}{\partial\tilde{U}} - \frac{dV_{DW}}{d\phi}\frac{\partial\phi}{\partial\tilde{U}} - \frac{\partial\kappa'}{\partial\phi}\frac{\partial\phi}{\partial\tilde{U}}\tilde{U}_{,i}\tilde{U}_{,i}. \quad (22)$$

Assume  $\phi = \phi(\tilde{U})$  then

$$\frac{\partial\tilde{U}}{\partial t} = \frac{\partial\phi/\partial t}{d\phi/d\tilde{U}}, \quad (23)$$

and,

$$(\kappa'\tilde{U}_{,i})_{,i} = \left(\frac{\kappa'\phi_{,i}}{d\phi/d\tilde{U}}\right)_{,i} = \frac{1}{d\phi/d\tilde{U}}(\kappa'\phi_{,i})_{,i} + \left(\frac{1}{d\phi/d\tilde{U}}\right)_{,i}\kappa'\phi_{,i}. \quad (24)$$

Finally

$$\left(\frac{1}{d\phi/d\tilde{U}}\right)_{,i} = -\frac{d^2\phi/d\tilde{U}^2}{(d\phi/d\tilde{U})^3}\phi_{,i}. \quad (25)$$

Substituting Eqs. (23)–(25) into Eq. (22)

$$\rho\Omega_1\frac{\partial\phi}{\partial t} = (\kappa'\phi_{,i})_{,i} - \frac{\partial\kappa'}{\partial\phi}\phi_{,i}\frac{d^2\phi/d\tilde{U}^2}{(d\phi/d\tilde{U})^2} - V_{DW}(\phi)(d\phi/\tilde{U})^2 - \frac{1}{2}\frac{\partial\sigma_{ij}}{\partial\phi}\varepsilon_{ij}(d\phi/d\tilde{U})^2. \quad (26)$$

The variable  $\phi$  is a function of  $\tilde{U}$  that still needs to be determined. Eqs. (13a), (13b), and (26) are the governing equations.

For the function  $\phi(\tilde{U})$  consider periodic interatomic potentials following the Peierls-Nabarro model [33–35] as shown in Fig. 1 below.

The abscissa shows the normalized displacement between atoms  $\tilde{U}/a$ , where  $a$  is the interatomic distance. Assuming a periodic variation of the interatomic potentials  $W$ , one can approximate it as follows:  $W = W_0\left(1 - \cos\left(2\pi\frac{\tilde{U}}{a}\right)\right) = 2W_0\sin^2\left(\pi\frac{\tilde{U}}{a}\right)$ , where  $2W_0$  represents the value of the potential energy barrier. The first derivative of the interatomic energy provides the expression for the internal forces:  $F = -\frac{\partial W}{\partial\tilde{U}} = -\frac{2\pi}{a}W_0\sin\frac{2\pi\tilde{U}}{a}$ . The equilibrium position corresponds to the places where  $F = 0$ . Stable equilibrium corresponds to the positions occupied by atoms  $\tilde{U}/a = k$ , where  $k$  is any integer. Unstable equilibrium positions correspond to  $\tilde{U}/a = \frac{1}{2} + k$  and an example is marked with a star in the Fig. 1. The stiffness of the system is defined as a derivative of the forces with respect to displacement, and, hence, is given by the second derivative of the potentials, i.e.  $E = \frac{\partial^2 W}{\partial\tilde{U}^2} = \frac{4\pi^2}{a^2}W_0\cos\frac{2\pi\tilde{U}}{a}$ . The values, where the stiffness equals to zero reflect the loss of stability (the stiffness cannot be negative), and subsequently, correspond to bifurcation, or, in fracture mechanics consideration, micro-cracking or damage. Thus, the bifurcation criterion is  $E = 0$  and becomes  $\tilde{U}/a = \pm\frac{1}{4} + k$ . The square in Fig. 1 illustrates the loss of stability due to the negative stiffness. It is also indicative of the physical limitation of stable micromechanical displacements. Hence, it allows for correlating the random displacement with the phase indicator.

For the sake of simplicity we will linearize the relationship between phase indicator (or damage variable)  $\phi$  and the relative

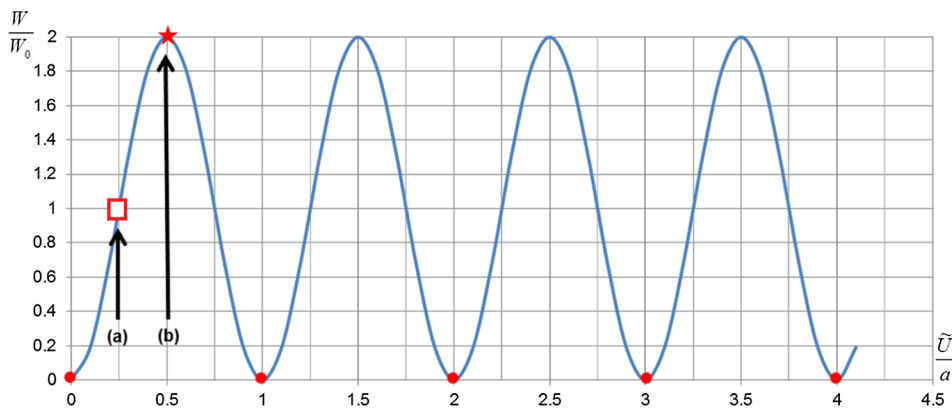


**Fig. 1.** Schematic illustration of interatomic potentials. Square symbol shows example of points where the stiffness has vanished (a), which occur at  $\tilde{U}/a = 1/4 + k$ ,  $k = 1, 2, 3, \dots$  and star symbol shows example of points where the internal forces are balanced (b),  $\tilde{U}/a = 1/2 + k$ ,  $k = 1, 2, 3, \dots$ . Points with solid circles are stable equilibrium while points marked by a star are unstable.

displacement  $\tilde{U}/a$ . Based on the considerations above, one can write,  $\begin{cases} \frac{\tilde{U}}{a} = 0, & \phi = 1, \text{ solid materials} \\ \frac{\tilde{U}}{a} = \frac{1}{4}, & \phi = 0, \text{ cracked materials} \end{cases}$ .

A linear approximation of the relationship of the following form was chosen for the sake of simplicity:

$$\frac{\tilde{U}}{a} = \frac{1}{4}(1 - \phi) \quad (27)$$

which can be inverted to yield

$$\phi(\tilde{U}) = 1 - 4\tilde{U}/a. \quad (28)$$

After substitution of (27), Eq. (26) becomes

$$\rho\Omega_1 \frac{\partial\phi}{\partial t} = (\kappa_{ij}\phi_j)_{,i} - \frac{16}{a^2}V'_{DW}(\phi) - \frac{8}{a^2} \frac{\partial\sigma_{ij}}{\partial\phi}\varepsilon_{ij}. \quad (29)$$

The equation can be simplified by redefining the constants. Let  $E_0 = \rho a^2\Omega_1^2/16$ ,  $\bar{\tau}_1 = 1/\Omega_1$  and  $\kappa = \kappa'a^2/16$ . Then

$$E_0 \bar{\tau}_1 \frac{\partial\phi}{\partial t} = (\kappa_{ij}\phi_j)_{,i} - V'_{DW}(\phi) - \frac{1}{2} \frac{\partial\sigma_{ij}}{\partial\phi}\varepsilon_{ij}. \quad (30)$$

For the parameter  $\kappa_{ij}$  we will use

$$\kappa_{ij} = D_0\delta_{ij} + D_1n_i n_j \quad (31)$$

where  $D_0$  and  $D_1$  are material parameters and  $n_k$  is a unit normal vector in the direction of the minimum principal stress. For example, in a two-dimensional stress state with the crack propagating along the x-axis the maximum principal stress will be in the y-direction and the minimum will be in the x-direction. Hence the parameter  $\kappa_{ij}$  will amplify the  $\vec{\nabla}\phi$  along the propagation direction. For example, in Mode I the minimum principle direction is along the crack and the phase will grow rapidly along the direction of the crack. If shear load is applied the principle direction is at 45° and the crack will change direction from along the original crack. It has been previously shown that the crack begins to propagate at 69° to the original crack direction [36,37]. The dependence of  $\kappa_{ij}$  on principal stress will produce extra terms in the equilibrium Eq. (13a), but we will use an existing finite element code for the stress and strain predictions and hence these extra terms are automatically included. Since the variation of  $\phi$  was used to find (30) and  $\kappa_{ij}$  does not depend on  $\phi$ , (30) does not need to be modified.

### 3. Definition of the parameters

Using  $D_0 = 0$  in Eq. (31) and considering representative cases where the crack propagates only in x-direction due to tensile loading in y-direction, Eq. (30) can be written as,

$$E_0 \bar{\tau}_1 \frac{\partial\phi}{\partial t} = D_1 \frac{\partial}{\partial x_i} \left( n_i n_j \frac{\partial\phi}{\partial x_j} \right) - V'_{DW}(\phi) - \frac{1}{2} \frac{\partial\sigma_{ij}}{\partial\phi}\varepsilon_{ij} \quad (32)$$

The diffusion coefficient  $D_1$  and  $V_{DW}$  can be defined using the following formulation [38,39] and has been described in Appendix B.

$$D_1 = \gamma\varepsilon, V_{DW} = \frac{\gamma}{\varepsilon}V_{pot}(\phi) \quad (33)$$

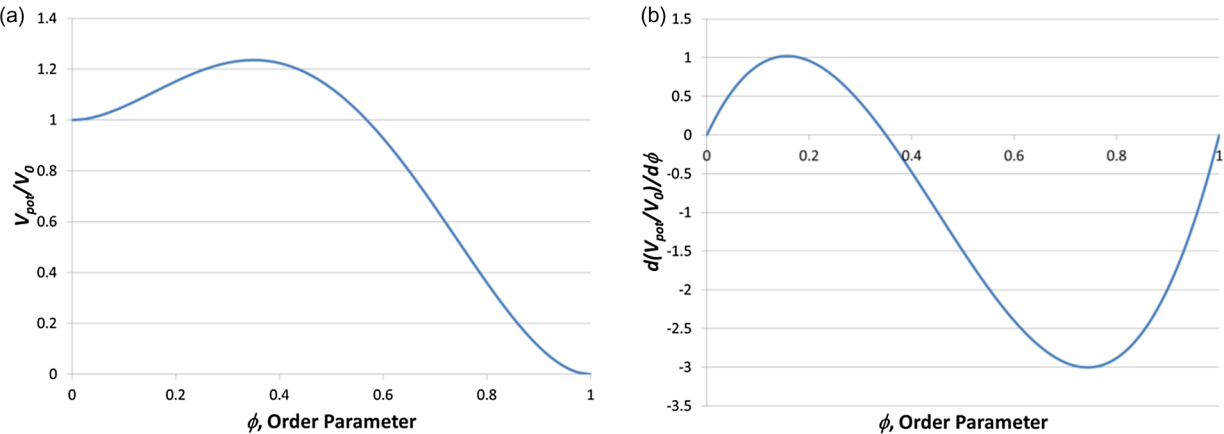
where  $\gamma$  is the crack resistance, or surface energy, and  $\varepsilon$  represents the interface thickness.  $V_{pot}(\phi)$  is expressed as,

$$V_{pot} = V_0(1 - \phi)^2(1 + 2\phi + C\phi^2) \quad (34)$$

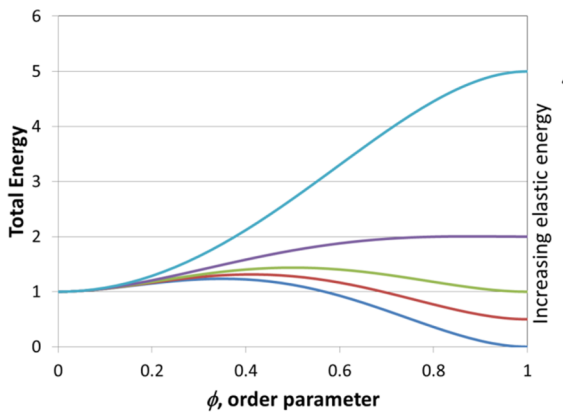
The role of the double well potential on evolution of the order parameter can be understood by inspecting Eq. (34) and corresponding graph in Fig. 2(a) for  $C = 10$ . As shown, there are two stable positions for the phase of the material that correspond to local minima of potential. These are at state corresponding to zero (completely failed) and one (intact). Also, it is important to note that the local minimum at  $\phi$  equal to zero is higher than the local minimum at  $\phi = 1$ . The actual function used in the evolution equation is the derivative of the double well potential function with respect to order parameter as shown in Fig. 2(b). The double well potential term will act to hold the phase at zero or one, or push the phase towards zero or one. For example, when the phase is just below one, the derivative becomes negative, therefore forcing the phase back to 1.

Fig. 3 is the plot of the sum of the double well potential and strain energy. From this plot we can see that as the strain energy increases the local minimum formed by the intact state ( $\phi = 1$ ) in the double well potential is lost [38]. This means when the strain energy is sufficiently large it can only drive towards the cracked state or  $\phi = 0$ .

In order to stop diffusion of the phase parameter from weaker singularities not associated with the crack tip, a cut off is used in the diffusion coefficient. The cut off is based on the fact that local principal stress near to the crack tip is much higher than away from it. The cut off multiplier modifies the diffusion coefficient by a factor,  $\lambda_1 = H(\sigma_1 - \beta\cdot\sigma_{app})$ , where,  $H$  is the Heaviside function,  $\sigma_1$  represents the 1st principal stress and  $\sigma_{app}$  represents the applied far-field stress, and  $\beta$  is a fitting coefficient reflecting strength of



**Fig. 2.** (a) Graph of double well potential for  $C = 10$  and (b) derivative of double well potential for  $C = 10$ .



**Fig. 3.** Plot of total energy (double well + strain energy) as function of order parameter.

singularities and taken in this work to be two.

To prevent crack healing, we have to eliminate the diffusion of the order parameter toward unity under compression. It was done by introducing another factor  $\lambda_2$  as follows:  $\lambda_2 = H(\sigma_1)$ .

Hence,

$$D_1 = \lambda_1 \lambda_2 \gamma \varepsilon \quad (35)$$

In this work we use materials parameters corresponding to Al 2000 series. The phase field parameters used and the material properties are shown in Table 1 [40].

#### 4. Results of the numerical studies

We apply the derived equations, using COMSOL [41], to several crack problems and compare the phase field predictions against classical fracture mechanics solutions. It is important to note that typical fracture mechanics results predict critical loads and displacements but crack propagation and crack trajectory predictions require additional significant numerical efforts. Phase field naturally predicts the propagation path. We analyze in this work the solution behavior near the critical loads, i.e. compare the crack

**Table 1**  
Phase field parameter and material properties used.

Young's modulus ( $E$ )	70 GPa
Poisson's ratio ( $\nu$ )	0.294
$C$	10
$\beta$	2
$E_0 \cdot \bar{\tau}_1$	$200 \text{ J sec/m}^3$
Surface energy ( $\gamma$ )	$5688.753 \text{ J/m}^2$
Fracture toughness ( $K_{1c}$ )	$20.88 \text{ MPa}\sqrt{\text{m}}$

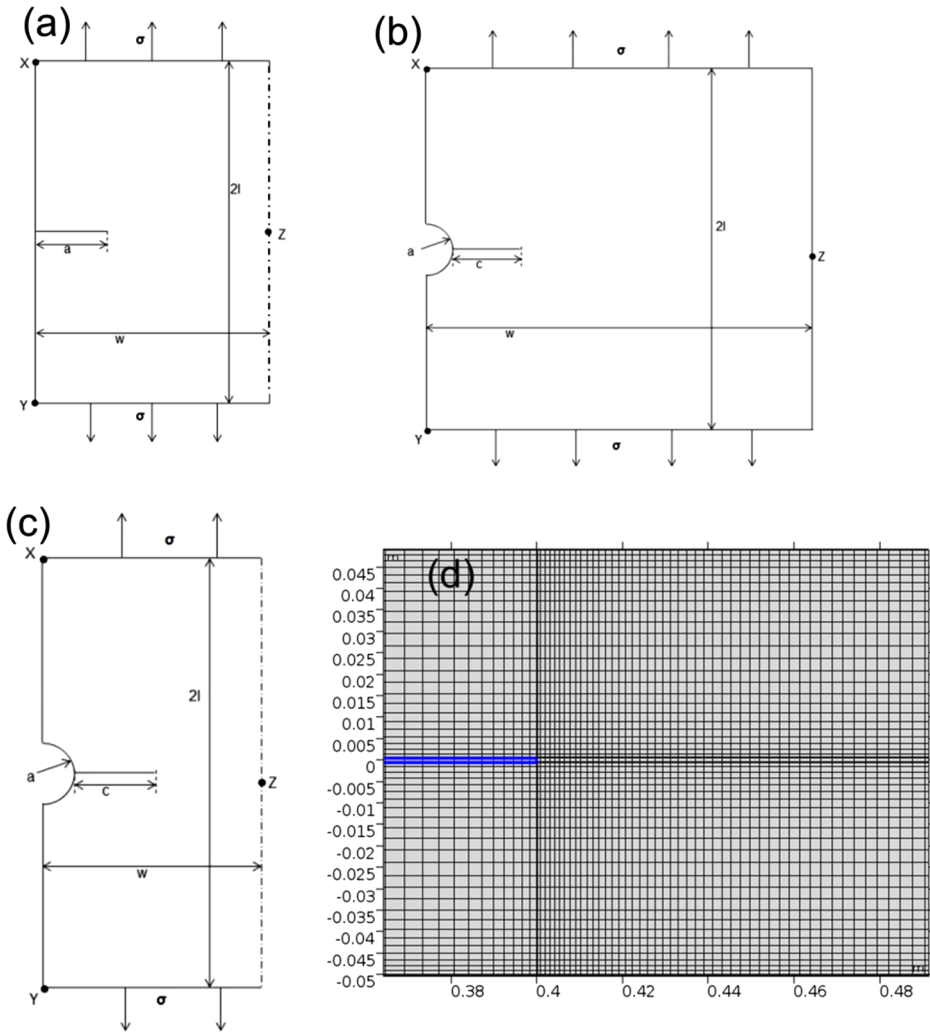


**Fig. 4.** Crack configuration for (a) case 1, (b) case 2, (c) case 3, and (d) representative grid used in front of the crack tip.

growth, and crack arrest conditions and compare them with fracture mechanics solutions. Three different crack configurations are investigated in the present study. The initial configuration, grid details and solution strategies are described below. The geometry of the crack configuration is shown in Fig. 4(a)–(c) along with the loading condition and the grid used in front of the initial crack tip is shown in Fig. 4(d). The mesh is generated so that the grid spacing in front of the crack tip is one order of magnitude smaller as compared to the interface thickness;  $\varepsilon$ . For all cases considered, the crack surface is modeled as a Dirichlet boundary condition of  $\phi = 0$  and at all the edges, zero flux boundary conditions are applied for  $\phi$ .

#### 4.1. Numerical cases

Case 1: Double Edge crack in the rectangular plate. We compare phase field solution to the well-known fracture mechanics solutions of [42,43].

A tensile load of  $\sigma$  is applied on the top and bottom edges as shown in Fig. 4(a). The left edge of the plate is free from external load while right edge is modeled as symmetry. Corner points X and Y are constrained in order to prevent X-displacement and constraint at point Z is used to prevent any Y-displacement. We also discuss the case when concentrated forces applied to crack surfaces. It allows us to check the crack growth, stability, and arrest.

Case 2: The problem of cracks emanating from holes or pores is extremely important in engineering practice. Stress concentration caused by a hole affects the crack initiation and propagation significantly reducing structural life. This is well a studied crack problem, analyzed by various numerical methods [44–46].

The geometry of the crack of length ' $c$ ' emanating from the hole of the radius ' $a$ ' is shown in Fig. 4(b). We report the results for four different relative crack lengths defined by  $c/a$  values of 0.2, 0.5, 1 and 2 correspondingly. Here, we chose the part geometry by assuming  $l/a = 10$  and  $w/a = 40$ . Such values are used to reduce any influence of the boundary surfaces on the crack. Finally

$a = 0.2\text{ m}$  is used for all the cases. Loading condition and constraints are the same as in Case 1.

Case 3: The geometry of the crack configuration is shown in Fig. 4(c), corresponding to interacting cracks emanating from pores; for a fracture mechanics solution, see, for example [47]. Two different crack lengths are studied so that  $c/a$  values are 0.4, and 0.8. Here,  $l/a = 12$  and  $w/a = 10$  are used and the right edge is modeled as a symmetry surface. Finally  $a = 0.25\text{ m}$  is used for all the cases. A tensile load of  $\sigma$  is applied on the top and bottom edges as shown in Fig. 4(c). The left edge acts as free surface and right edge is modeled as symmetry. Similar to case 1 and 2, corner points X and Y are used to prevent any X-displacement and Z is used to prevent any Y-displacement.

#### 4.2. Crack propagation

Propagating crack shapes for the straight crack configurations (cases 1, 2 and 3) are shown in Fig. 5. Fig. 5(a) and (b) show the crack growth for case 1. The blue region in Fig. 5(a) indicates the initial crack and Fig. 5(b) shows how the crack diffuses into the undamaged region (red colored). At the interface the order parameter  $\phi$  varies from 0 to 1 and  $\phi = 0.5$  is used to track the instantaneous crack position at any time. Fig. 5(c) and (d) shows propagation of straight crack initiated from a hole. As seen in Fig. 5(d) there is no diffusion observed near the hole surface, but the crack emanating from the hole does grow. A similar trend is observed from Fig. 5(e) and (f), which shows crack propagation for case 3.

The far field stress in the intact phase ( $\phi = 1$ ) is just solution of equilibrium equations and independent of phase field. Hence, it should match exactly the fracture mechanics solution. However, near the crack tip ( $0 < \phi < 1$ ), the material properties vary depending on the phase indicator, which cannot be captured by fracture mechanics. As can be seen in Fig. 6, the difference between phase field and fracture mechanics solutions rapidly decreases with increasing distance from the crack tip.

The asymptotic approximation of normal stress near tip of a mode I crack is

$$\sigma_{yy} = \frac{K_I}{\sqrt{2\pi r}} \cos \frac{\theta}{2} \left( 1 + \sin \frac{\theta}{2} \sin \frac{3\theta}{2} \right), \quad (36)$$

where  $K_I$  is stress intensity factor (SIF) and  $(r, \theta)$  is the polar coordinates with origin at the crack tip and crack surfaces correspond to  $\theta = \pm \pi$ . SIF is determined for this specific geometry as [42,43]:

$$K_I = \sigma \sqrt{2W \tan \left( \frac{\pi a}{2W} \right)} F \left( \alpha, \frac{l}{W} \right); \quad \alpha = \frac{a}{W}; \quad (37)$$

where  $F \left( \alpha, \frac{l}{W} \right)$  is monotonically increasing correction function tabulated in [42,43]. Finite element solutions of the equilibrium Eq. (13a) coupled with phase field Eq. (30) predicts the complete stress field, which is compared against the asymptotic near crack tip approximation of  $\sigma_{yy}$  in Eqs. (36) and (37) on Fig. 6. Fig. 6(a) shows the stress field in front of the crack tip ( $\theta = 0$ ) and Fig. 6(b) illustrates variation of the  $\sigma_{yy}$  with polar angle  $\theta$  at some fixed distance from the crack tip (here was taken  $r = 0.03$ ). The error of the predictions does not exceed 2%, demonstrating that even the asymptotic solution has been evaluated accurately.

#### 4.3. Crack propagation criteria and comparison with fracture mechanics

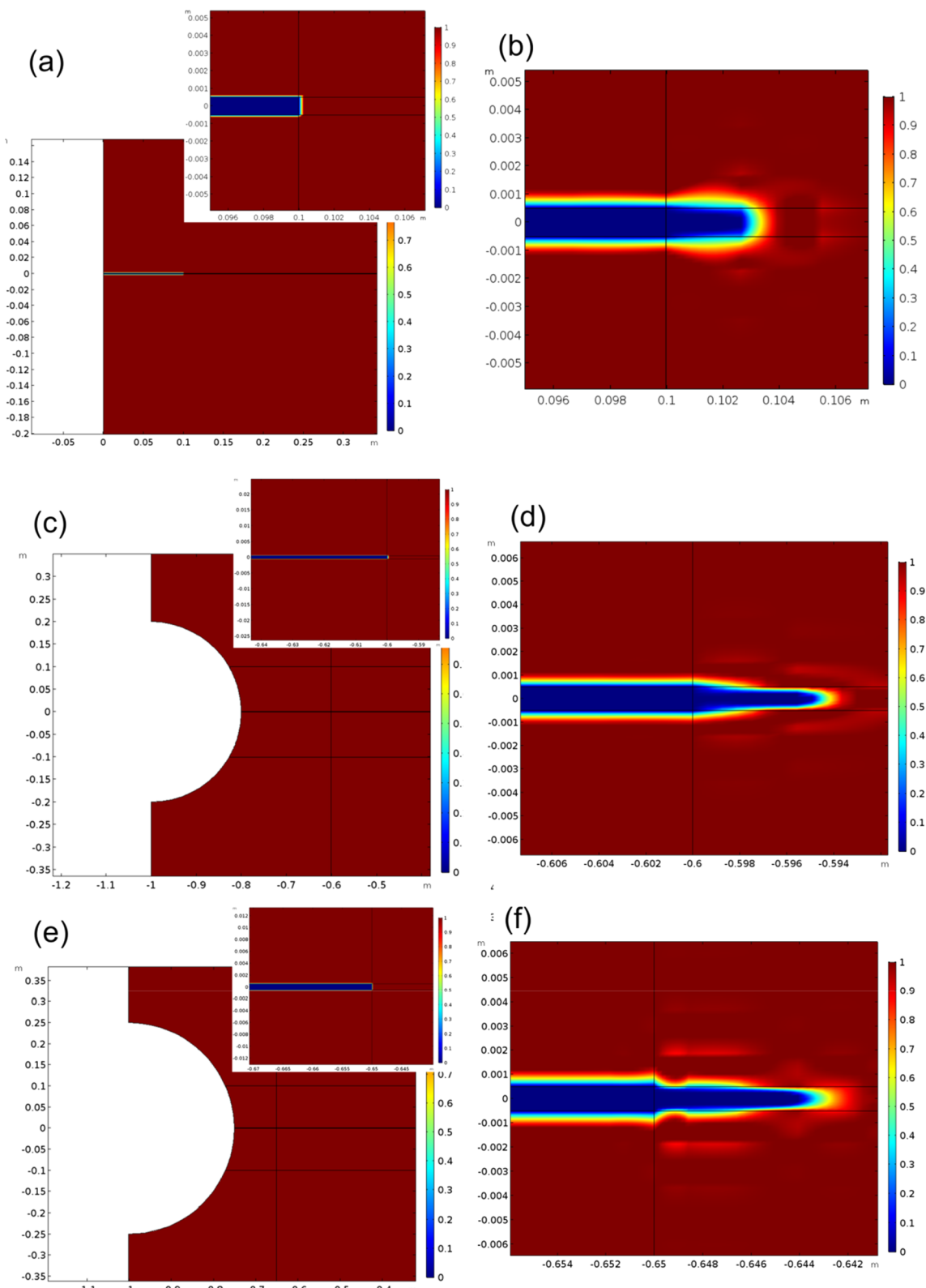
Phase field analyses of crack propagation were run by varying the applied stress for all the crack configurations described. The goal is to understand if the critical stress value for each crack configuration can be deduced from the variation of order parameter. To compare the simulation results with fracture mechanics based predictions, two different approaches are proposed. The 1st approach relies on evaluation of the crack propagation velocity. The crack tip velocity can be written as,

$$V_c = - \frac{\left| \frac{\partial \phi}{\partial t} \right|}{\sqrt{\left( \left( \frac{\partial \phi}{\partial x} \right)^2 + \left( \frac{\partial \phi}{\partial y} \right)^2 \right)}} H(0.5 - \phi) \quad (38)$$

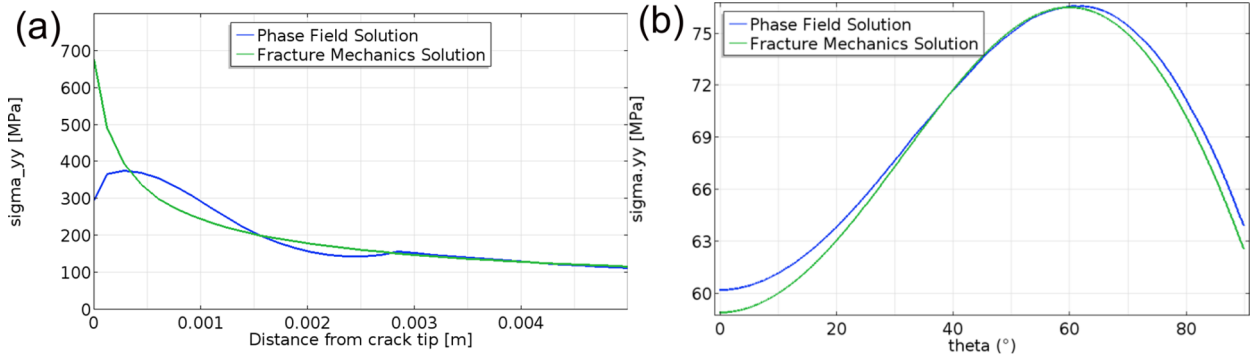
where the Heaviside function is used to track the interface between cracked and undamaged regions. The velocity in Eq. (38) is tracked for all the cracks considered at the time instants that are chosen in such a way that the interface crosses the 1st grid element beyond the crack tip.

Fig. 7 shows the crack tip propagation velocity as functions of applied stresses for the cracks described in case 1. From dimension analysis of Eq. (32), one can see that the characteristic velocity should be of the order of  $D_1/E_0\tau_1 l_c = \gamma_e/E_0\tau_1 l_c$ , where  $l_c$  is characteristic size.

It is important to note that we do not solve the dynamic (hyperbolic) equations that predict the speed of the crack tip to be equal to the Rayleigh wave velocity if the applied stress exceeds the critical value and zero if the stress is less than the critical one. In the phase field approach, the parabolic equation for the phase parameter is considered as a suitable approximation for crack growth prediction. As expected, the calculated crack tip velocity monotonically increases with stresses and is not equal to zero even for small loads. Velocity continuously rises with applied stresses with no jumps. Fig. 7 illustrates the result that predicted crack tip normalized velocity is close to 1 if critical stress is applied. The velocity increases very fast (an order of magnitude) under higher stress values. As can be seen from this example, the phase field based solution is able to capture the same value of the crack tip propagation velocity near the applied critical stress; hence, the value of the velocity may be used as an approximate indicator of actual crack propagation or arrest. At high stress and high initial crack length the velocity deviates from a monotonically increasing trend. This is probably



**Fig. 5.** Initial crack configuration for (a) case 1, (c) case 2 and (e) case 3 and crack shape at later time instant for (b) case 1, (d) case 2 and (f) case 3. Blue color indicates  $\phi = 0$  or cracked region and red color indicates  $\phi = 1$  or undamaged region. (For interpretation of the references to color in this figure legend, the reader is referred to the web version of this article.)



**Fig. 6.** Comparison of numerically predicted and fracture mechanics solution of  $\sigma_{yy}$  for case I ahead of crack tip at 0.2025 m as a function of (a) distance and (b) polar angle  $\theta$  from the crack direction.

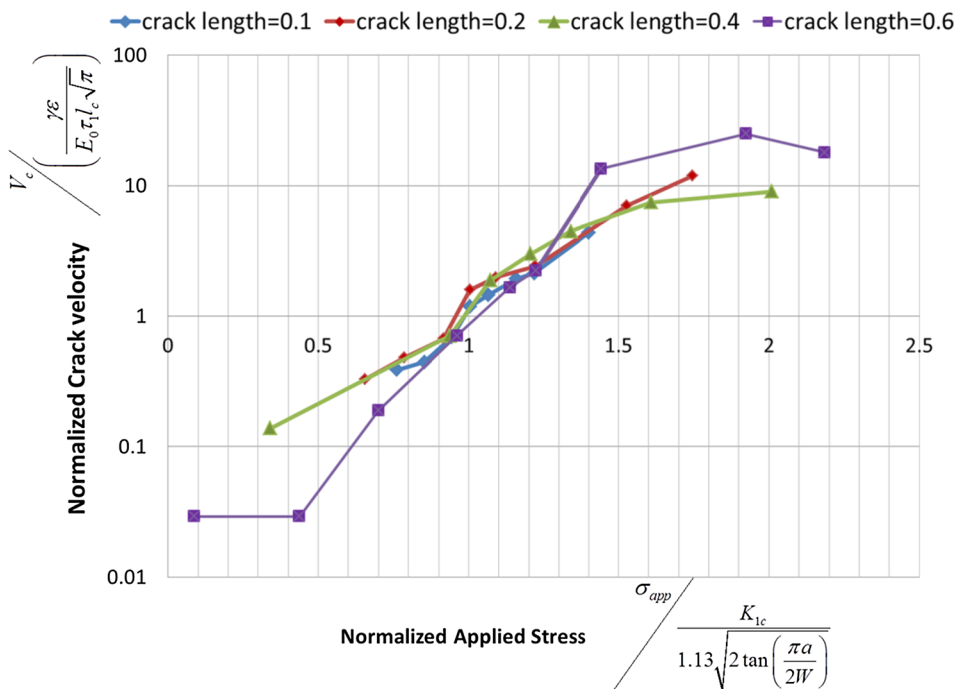


**Fig. 7.** Calculated normalized crack tip propagation velocity vs normalized applied stress for various initial crack lengths.

associated with crack bifurcation observed near these parameters and is discussed in Section 4.4.

Velocity estimation is fast and easy but not always an accurate criterion to evaluate when the applied load reaches the critical value and the crack actually propagates, which is critical information for any practical analysis.<sup>1</sup> Another approach relies on the evaluation of the elastic strain energy density around the crack tip. This approach is found to be less time-dependent in nature and the integral over the path is compared with the analytically evaluated value. The elastic energy density is always calculated during numerical procedures, so the value of  $\oint Wdl = \oint \frac{1}{2} \sigma_{ij} \epsilon_{ij} dl$  is readily evaluated. Fracture mechanics provides the value of such an integral in the near vicinity of the crack tip (see Appendix C for details), which equals, for example, for Mode I cracks,  $\oint Wdl = \frac{(1+\nu)(5-8\nu)K_I^2}{8E}$ . Hence, one can compare the value of the integral calculated in the current mesh of “phase-field” crack predictions against  $\frac{(1+\nu)(5-8\nu)K_{1c}^2}{8E}$  in order to determine if the applied stress reaches the critical value and the crack propagates.

The comparisons of different approaches with fracture mechanics solutions are shown in Table 2. The case 1 solutions are tabulated in Table 2 and case 2 and 3 solutions along with comparison with fracture mechanics study are presented in Table 3. As seen, both methods predicted critical stress in same order for most of the trials.

One can see that the value of critical stress calculated by contour integration for small crack lengths is less accurate than for longer

<sup>1</sup> It is interesting to note that the equation parameters can be adjusted in such a way to fit fatigue crack growth rate, allowing fatigue prediction using phase field approach.

**Table 2**

Comparison of phase field prediction with fracture mechanics results for loading case 1.

Trial number	Crack configuration	Crack length (normalized)	Critical stress from fracture mechanics (MPa)	Critical stress from velocity study (MPa)	Critical stress from contour integral (MPa)
1	Straight crack	0.1	32.83	32	31
2		0.2	22.92	23	23
3		0.4	14.93	16	14
4		0.6	11.44	12	11

**Table 3**

Comparison of phase field prediction with fracture mechanics results for loading cases 2 and 3.

Trial number	Crack configuration	Crack length		Critical stress from fracture mechanics (MPa)	Critical stress from velocity study (MPa)	Critical stress from contour integral (MPa)
		a	c			
5	Single edge cracked from circle	0.2	0.04	23.64	24	21
6		0.2	0.1	19.46	18	18
7		0.2	0.2	16.56	15	15
8		0.2	0.4	13.45	13	12
9	Double edge cracked from circle	0.25	0.1	18.3	18	18
10		0.25	0.2	15.7	16	16

ones. This is a numerical artefact caused by the influence of the free boundary.

Similar solutions have been obtained for point force loads under mode I. The results are compared with the fracture mechanics solution given by [48],

$$K_I = \frac{2.589P}{\sqrt{\pi a}} \quad (39)$$

In this case the crack propagation is stable because of  $\frac{\partial K_I}{\partial a} < 0$ . The stable crack length computed from this formula based on material fracture toughness ( $K_{IC}$ ) and applied load ( $P$ ) can be used to predict how crack will progress before its arrest occurs. A straight crack configuration with geometry of trial number 2 is adopted and Eq. (39) used to predict crack arrest at 0.493 mm for a point load of 6400 kN. To avoid the singularity at point load, the load is distributed over a length of 1 mm. Simulation results in Fig. 8 show that the normalized crack tip velocity,  $\frac{V_c}{(\gamma/E_0 \tau_1 c \sqrt{\pi})}$ , (where  $V_c$  represents velocity of crack tip in m/s) evaluated at  $\phi = 0.5$ , reduces below 1 at crack tip horizontal location position = 0.49 mm. Hence, the described phase field calculations together with critical stress/crack propagation evaluation criteria can accurately predict crack propagation and arrest, which is essential for engineering applications

#### 4.4. Non-straight cracking

To extend this method for a non-straight crack, the pure shear problem is solved and the solution is presented in Fig. 9. Without the ramp factor  $\lambda_1$  and  $\lambda_2$ , the crack also grows in the compressive stress zone as shown in Fig. 9(b). With the introduction of  $\lambda_1$  and  $\lambda_2$ , the crack propagates under in the tensile stress regime. Of particular importance, is that the simulated crack shows the initial

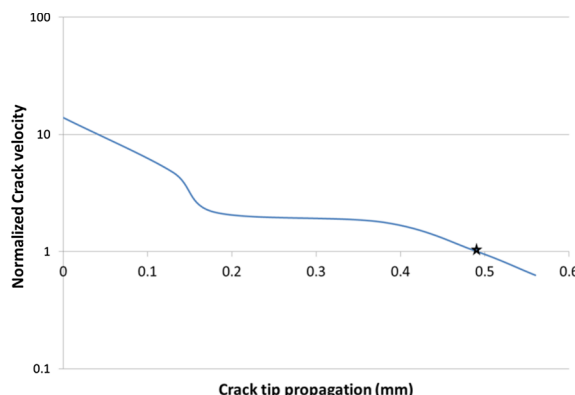


**Fig. 8.** Plot of velocity vs. crack tip propagation for a point loading of 6400 kN and initial crack length = 0.2 m. Star indicates fracture mechanics solution for crack arrest at 0.493 mm.

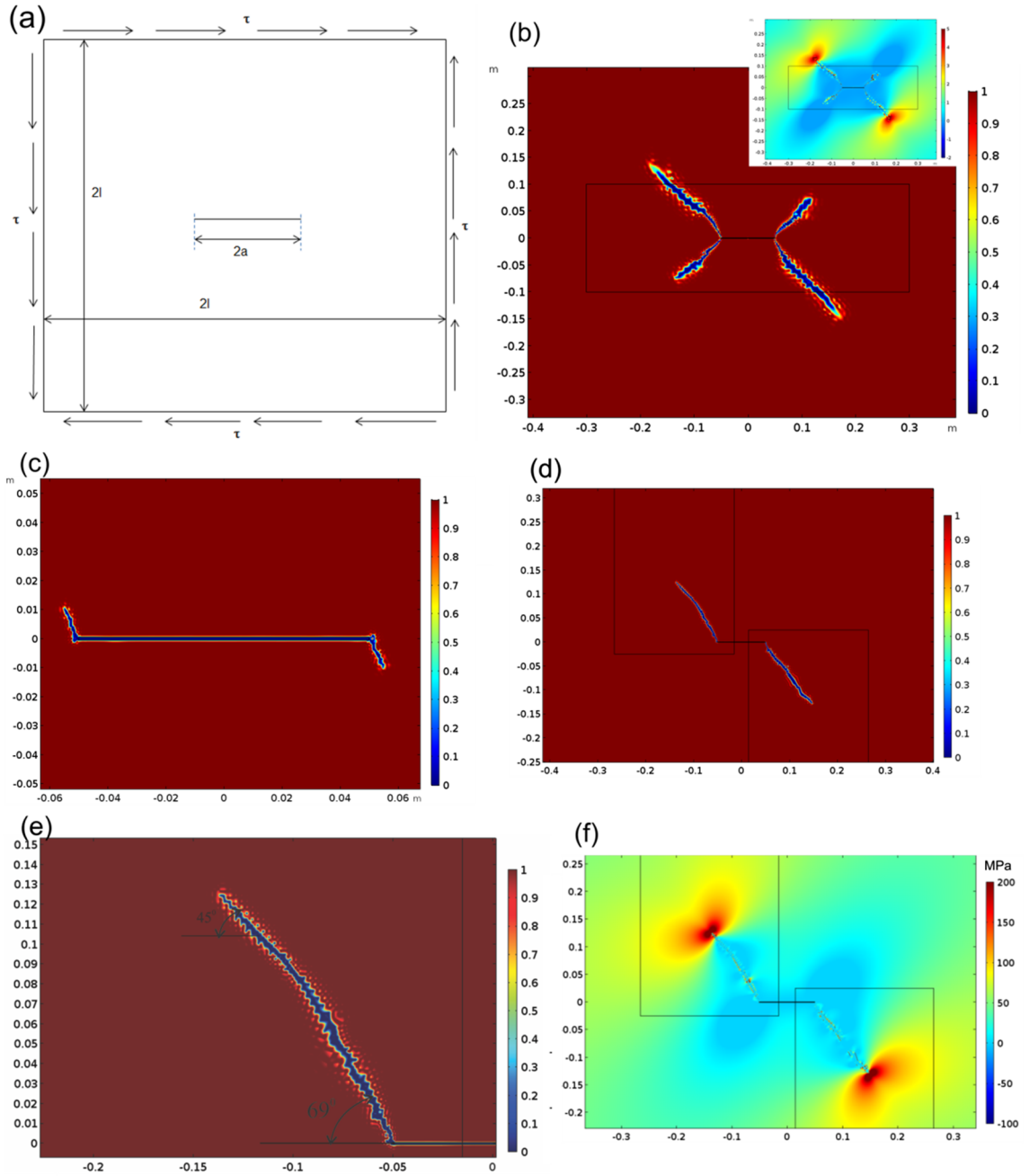


**Fig. 9.** (a) geometry and boundary load configuration for pure shear case, (b) crack propagation in absence of factor  $\lambda_2$ , (c) initial angle for the crack and (d) final crack configuration after turning, (e) measured angle in shear crack and (f) stress distribution.

fracture angle to be within 69–70°, which agrees well with results from fracture mechanics modeling and experiments [36,37,49]. Also, the bending of crack to 45° can be observed upon further growth, which is expected because crack finally aligns itself perpendicular to the maximum principal stress.

The calculated critical values of shear stress appeared to be equal to 48 MPa for the material parameters and geometry shown and discussed above. This value is calculated by the use of contour integration  $\oint W_{el} dl$  for the shear crack mode but comparing it against the asymptotic value for the integral  $\frac{(1+\nu)(9-5\nu)K_c^2}{8E}$ . According to LEFM, initial branching is described by a singular integral equation [50], which can be reduced to finding the asymptotes of SIF for small, in comparison to the initial crack, branches of length  $l(\frac{l}{a} \rightarrow 0)$  [51]. The principal terms of this asymptotic expansion (for  $K_I$ ) may be taken as the shear crack propagation criterion. Based on the criterion that cracks will propagate in the direction  $\Theta$  maximizing the value of  $K_I(\Theta)$  at the tip of the infinitesimal branch when

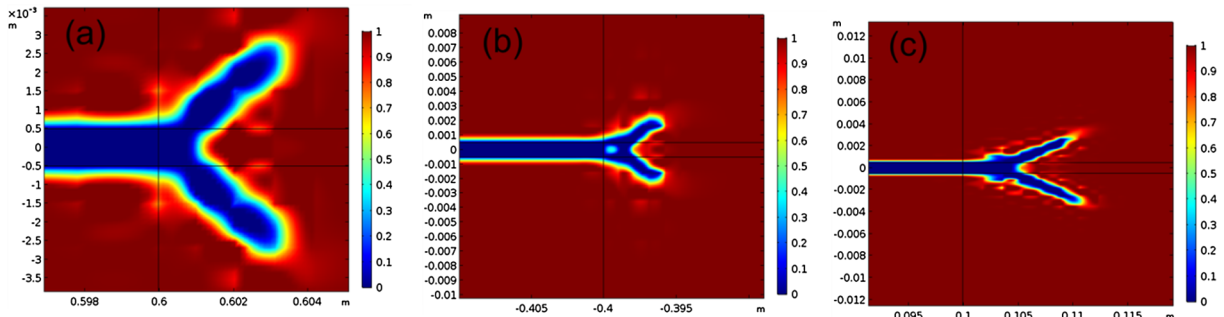


**Fig. 10.** Bifurcation observed for various loading conditions corresponding to (a) case 4, (b) case 8 and (c) case 1.

$K_I(\Theta) = K_{IC}$  is satisfied. The value of the critical stress should be  $\tau_c = \frac{K_{IC}}{1.18\sqrt{\pi a}}$ , which equals to 45 MPa for given values of  $K_{IC}$  and crack length  $a$ .

The straight cracks presented in Figs. 4 and 5 are prone to bifurcation. In our calculations bifurcation happens when the crack propagation velocity increases almost an order of magnitude and the energy density term increases correspondingly. This observation is presented in Fig. 10. Simulations with large initial crack length cases are found more prone to bifurcation (Fig. 10(a, b)), while simulations with smaller crack length show bifurcation as the crack progresses some distance (Fig. 10c). It is important that LEFM meets serious technical and conceptual difficulties in attempts to predict crack bifurcation [36,52], and requires additional assumptions.

Our simulations showed that after a crack bifurcates the velocity continues to increase. Hence, the phenomenon is not a result of a maximum in the wave speed. This is similar to the observation in flow fingering [53]. It is important to note that the stress state is calculated for steady state conditions ( $\sigma_{ij,j} = 0$ ) and does not result from hyperbolic partial differential equations, but there is still a bifurcation instability. The equations in our simulations are parabolic in the phase and elliptic in the mechanical displacements and do not describe a wave propagation process. Existing descriptions attribute the bifurcation of cracks to the hyperbolic nature of the wave propagation equation [54,55]. It appears that hyperbolic equations are not necessary to describe crack bifurcation. An approach for predicting crack instability (bifurcation) would be to examine small oscillations over time and space of the phase and mechanical displacements in the governing parabolic phase equations and the elliptic displacement equations. Next step would be to look for frequencies that grow exponentially (that is the imaginary part of the frequency results in exponential growth). This needs much more work to complete and is a topic for a future study.

## 5. Discussion and concluding remarks

An action was developed from a Lagrangian density that includes a phase indicator. After setting the variation of the action to zero, the phase is shown to be governed by a diffusion equation. The diffusion equation is commonly used to represent non-deterministic processes and provides more accurate physical representations of probabilistic processes. Since crack growth is inherently a probabilistic process, the diffusion of the phase indicator can represent the spread in the crack location. The resulting equations were incorporated in a finite element code (COMSOL) and used to predict crack growth phenomena.

The phase-field based crack propagation approach is both computationally attractive and a physically motivated path for crack modeling. However, the choice of the model parameters and the validation for the phase field model assumptions is still not completely understood. Most of the work on phase-field crack growth predictions are theoretical and focused on crack path analysis. Comparison of the phase-field prediction against calibrated LEFM solutions and/or experiments are scattered and are mostly qualitative.

In this work we have compared the phase field predictions with well-established fracture mechanics solutions in order to validate phase-field crack propagation solutions and to take a step toward the development of engineering oriented crack propagation software tools. Parameters were developed for aluminum. We evaluated two schemes that can be used to compute critical stress value for a given crack configuration and compared the performance of the schemes with known fracture mechanics solutions. From the results shown in Tables 2 and 3, it can be concluded that the contour integral based scheme slightly underestimates the critical stress, while the velocity-based scheme slightly overestimates it. Both schemes are proven to be reasonably accurate in evaluating the critical stress and the maximum error is found to be on the order of 10%. The particular analysis has been performed for an aluminum alloy and accurately represented the actual values of critical stresses specific for this aluminum alloys. Crack paths were predicted with high accuracy, including bifurcation.

The results presented agree well with Fracture Mechanics but do not require re-meshing or special elements used in traditional crack propagation simulations, and, hence, are more efficient computationally. Crack arrest is also accurately predicted, which is very important for engineering reliability/safety analysis. It allows wide application of damage tolerant approaches in the design practice.

The presence of concentrated forces in our simulations caused numerical difficulties that could only be removed by spreading the force over several elements. Otherwise, singular stress field produced by concentrated force led to localized fast propagation of the phase field. Both velocity and energy evaluations were useful in the accurate prediction of critical stress values and crack

propagation. A particularly surprising result was the prediction of cracks bifurcating into two cracks without the addition of inertial effects. A method for predicting crack bifurcation for steady state stress distributions needs to be developed.

## Appendix A. Thermomechanical diffusion equation

Recall from Eq. (13b)

$$\zeta \rho \frac{\partial \tilde{u}}{\partial t} = (K' \tilde{u}_{,i})_{,i} - \frac{1}{2} \frac{\partial K'}{\partial \tilde{u}} \tilde{u}_{,i} \tilde{u}_{,i} + \frac{\partial \sigma_{ij}}{\partial (\partial \tilde{u} / \partial t)} \dot{\epsilon}_{ij}, \quad (A1)$$

where it is assumed that  $\partial \tilde{u} / \partial t = \tilde{u} / \zeta$  relates the random velocities to the rate of change of the random displacements. The thermal propagation speed is  $\sqrt{K' / (\zeta \rho)}$ . From molecular dynamics studies, [56], the thermal propagation speed is approximately  $\sqrt{\mu / \rho}$ . Then  $\zeta = K' / \mu \approx 2$ . (A2)

Using Eqs. (9)–(12) and (A2), (A1) becomes

$$\rho C_p \frac{\partial T}{\partial t} = (KT_{,i})_{,i} + T \frac{\partial \sigma_{ij}}{\partial T} \dot{\epsilon}_{ij}. \quad (A3)$$

This is exactly the transient thermal conduction equation [34] with mechanical effects. Note that it is clear from the derivation that the stresses not only vary with the temperature through the thermal strain, but also through the variation of the moduli,  $\mu$  and,  $\lambda$  and the thermal expansion coefficient,  $\alpha$ , with temperature.

## Appendix B. Phase field parameters determination

The total energy of the system  $F(\phi, \vec{u})$  can be written following Eqs. (32) and (33) as,

$$F(\phi, \vec{u}) = \int \left[ \gamma \left( \varepsilon |\nabla \phi|^2 + \frac{1}{\varepsilon} V_{pot} \right) + g(\phi) f_{el} \right] dV \quad (B1)$$

Here,  $f_{el}$  represents strain energy density, and  $g(\phi)$  can be expressed as,

$$g(\phi) = 4\phi^3 - 3\phi^4 \quad (B2)$$

reflecting the dependence of elastic properties on the phase indicator. According to [39], for one-dimensional system of 2L in length ( $L = 1$  m), the profile of order parameter is characterized by the equilibrium state  $\phi = 0$ . Under unloaded condition, equipartition of the energy in Eq. (B1) gives,

$$\begin{aligned} 2\gamma \varepsilon \frac{\partial^2 \phi}{\partial x^2} &= \frac{\gamma}{\varepsilon} \frac{\partial V_{pot}}{\partial \phi} \Rightarrow 2 \int_0^x \frac{\partial \phi}{\partial x} \frac{\partial^2 \phi}{\partial x^2} dx = \frac{1}{\varepsilon^2} \int_0^x \frac{\partial \phi}{\partial x} \frac{\partial V_{pot}}{\partial \phi} dx \\ &\Rightarrow \left( \frac{\partial \phi}{\partial x} \right)^2 = \frac{V_{pot}}{\varepsilon^2} \Rightarrow \frac{\partial \phi}{\partial x} = \frac{1}{\varepsilon} \sqrt{V_{pot}} \end{aligned} \quad (B3)$$

In order to fulfill the Griffith criterion for the crack growth the interfacial energy from an interface must be equal as  $\gamma$  [57]

$$\gamma = \int_0^L 2\gamma \left[ \varepsilon \left( \frac{\partial \phi}{\partial x} \right)^2 + \frac{1}{\varepsilon} V_{pot} \right] dx \quad (B4)$$

Substituting for  $\frac{\partial \phi}{\partial x}$  in Eq. (B3), using  $\gamma = \frac{(1-\nu^2)}{E} K_{IC}^2$  (where  $E$  is Young's modulus) and  $V_{DW}$  from Eq. (33), we obtain the value of  $V_0$ :

$$V_0 = 0.0844, \text{ and also } L = \int_0^1 \frac{\partial x}{\partial \phi} d\phi = \frac{\varepsilon}{\sqrt{V_0}} \int_0^1 \frac{\partial \phi}{\sqrt{(1-\phi^2)(1+2\phi+C\phi^2)}} = 36.8727\varepsilon. \quad (B5)$$

## Appendix C. Path integrals for modes I, II and III

From the dimensional analysis it follows that the linear integral of the energy density should be proportional to the surface energy. We consider such an integral along a circular path around the crack tip with the radius small enough to assume a crack singular stress term accurate approximation for the stress field. Strain components for plane strain deformation are:

$$\varepsilon_{11} = \frac{1+\nu}{E} (\sigma_{11} - \nu(\sigma_{33} + \sigma_{22})),$$

$$\varepsilon_{22} = \frac{1+\nu}{E} (\sigma_{22} - \nu(\sigma_{33} + \sigma_{22}))$$

The other strain components are as follows:  $\varepsilon_{33} = 0$ ,  $\varepsilon_{12} = \frac{1+\nu}{E} \sigma_{12}$ ;  $\varepsilon_{13} = \varepsilon_{23} = 0$  and  $\sigma_{33} = \nu(\sigma_{11} + \sigma_{22})$ . The strain energy density is

$$W = \frac{1}{2} \sigma_{ij} \varepsilon_{ij} = \frac{1+\nu}{2E} [(1-\nu)(\sigma_{11} + \sigma_{22})^2 - 2\sigma_{11}\sigma_{22} + 2\sigma_{12}^2] \quad (\text{C1})$$

Now, let us use the asymptotic approximation of the stress field near tip of a mode I crack:

$$\begin{aligned} \sigma_{11} &= \frac{K_I}{\sqrt{2\pi r}} \cos \frac{\theta}{2} \left( 1 - \sin \frac{\theta}{2} \sin \frac{3\theta}{2} \right); \\ \sigma_{22} &= \frac{K_I}{\sqrt{2\pi r}} \cos \frac{\theta}{2} \left( 1 + \sin \frac{\theta}{2} \sin \frac{3\theta}{2} \right); \\ \sigma_{12} &= \frac{K_I}{\sqrt{2\pi r}} \cos \frac{\theta}{2} \sin \frac{\theta}{2} \cos \frac{3\theta}{2}. \end{aligned} \quad (\text{C2})$$

Substituting (C2) into the expression for elastic energy density (C1) one immediately obtains

$$W = \frac{(1+\nu)K_I^2 \cos^2 \frac{\theta}{2}}{2\pi E r} \left[ 1 - 2\nu + \sin^2 \frac{\theta}{2} \right].$$

Next, if we calculate  $\oint W dl$  using a circular contour around crack tip, we get

$$\oint W dl = \frac{(1+\nu)K_I^2}{2\pi E} \int_0^{2\pi} \cos^2 \frac{\theta}{2} \left( 1 - 2\nu + \sin^2 \frac{\theta}{2} \right) d\theta = \frac{(1+\nu)(5-8\nu)K_I^2}{8E} \quad (\text{C3})$$

As can be seen from (C3)

$$\oint W dl = \frac{(1+\nu)(5-8\nu)K_I^2}{8E} = \frac{(5-8\nu)}{8(1-\nu)} J_I \quad (\text{C4})$$

which equals to  $0.5J_I$  if  $\nu = 0.25$ .

Similar results can be obtained for shear and anti-plane crack modes:

$$\oint W_{II} dl = \frac{(1+\nu)(9-5\nu)K_{II}^2}{8E} = \frac{(9-5\nu)}{8(1-\nu)} J_{II} \text{ and } \oint W_{III} dl = \frac{(1+\nu)K_{III}^2}{E} = J_{III}.$$

## References

- [1] Bathe KJ. Finite element procedures. Englewood Cliffs, NJ: Prentice-Hall; 1996.
- [2] Du Zhen-Zhong. Extended Finite Element Method (XFEM) in Abaqus. Dassault Syst WWW 3ds Com/Plano Del Eje Ferrov Plano Del Eje Ferrov Plano Del Eje Ferrov; 2009.
- [3] Katsikadelis JT. The boundary element method for engineers and scientists: theory and applications. Academic Press; 2016.
- [4] Annigeri BS, Cleary MP. Surface integral finite element hybrid (SIFEH) method for fracture mechanics. Int J Numer Methods Eng 1984;20:869–85.
- [5] Forth SC, Staroselsky A. A hybrid FEM/BEM approach for designing an aircraft engine structural health monitoring. Comput Model Eng Sci 2005;9:287.
- [6] Staroselsky A, Cassenti BN. Creep, plasticity, and fatigue of single crystal superalloy. Int J Solids Struct 2011;48:2060–75.
- [7] Busse C, Palmert F, Sjödin B, Almroth P, Gustafsson D, Simonsson K, et al. Prediction of crystallographic cracking planes in single-crystal nickel-base superalloys. Eng Fract Mech 2018;196:206–23.
- [8] Antolovich BF, Saxena A, Antolovich SD. Fatigue crack propagation in single-crystal CMSX-2 at elevated temperature. J Mater Eng Perform 1993;2:489–95.
- [9] Kersey RK, Staroselsky A, Dudzinski DC, Genest M. Thermomechanical fatigue crack growth from laser drilled holes in single crystal nickel based superalloy. Int J Fatigue 2013;55:183–93.
- [10] Xu X-P, Needleman A. Numerical simulations of fast crack growth in brittle solids. J Mech Phys Solids 1994;42:1397–434.
- [11] Ingrafea T. FRANC3D, 3D fracture analysis code. NY: Cornell Univ Fract Group, Cornell Univ Ithaca; 1996.
- [12] Sharon E, Fineberg J. Confirming the continuum theory of dynamic brittle fracture for fast cracks. Nature 1999;397:333.
- [13] Cramer T, Wanner A, Gumbsch P. Dynamic fracture of glass and single crystalline silicon. Z Met 1999;90:675–86.
- [14] Ravi-Chandar K, Knauss WG. An experimental investigation into dynamic fracture: I. Crack initiation and arrest. Int J Fract 1984;25:247–62.
- [15] Broberg K. Cracks and fractures (Academic, New York, 1999); LB Freund, Dynamic Fracture Mechanics; 1990.
- [16] Freund LB. Dynamic Fracture Mechanics. Cambridge University Press Cambridge Google Scholar; 1990.
- [17] Adair BS, Johnson WS, Antolovich SD, Staroselsky A. Crystallographic orientation and temperature effects on the fatigue crack growth rate and resulting fracture surface morphology in PWA1484 single crystal superalloy. Fatigue Fract Eng Mater Struct 2015;38:56–68.
- [18] Kachanov LM. Introduction. Introd. to Contin. damage Mech. Springer; 1986. p. 1–10.
- [19] Lemaître J, Chaboche JL. Mechanics of solid materials. Cambridge University Press Cambridge; 1990. UK Google Sch.
- [20] Basaran C, Nie S. An irreversible thermodynamics theory for damage mechanics of solids. Int J Damage Mech 2004;13:205–23.
- [21] Lancioni G, Royer-Carfälli G. The variational approach to fracture mechanics. A practical application to the French Panthéon in Paris. J Elast 2009;95:1–30.
- [22] Bourdin B, Francfort GA, Marigo J-J. The variational approach to fracture. J Elast 2008;91:5–148.
- [23] Hakim V, Karma A. Laws of crack motion and phase-field models of fracture. J Mech Phys Solids 2009;57:342–68.
- [24] da Silva Jr MN, Duda FP, Fried E. Sharp-crack limit of a phase-field model for brittle fracture. J Mech Phys Solids 2013;61:2178–95.
- [25] Kuhn C. Numerical and analytical investigation of a phase field model for fracture; 2013.
- [26] Qin RS, Bhadeshia HK. Phase field method. Mater Sci Technol 2010;26:803–11.
- [27] Levitas VI, Idesman AV, Palakar AK. Phase-field modeling of fracture in liquid. J Appl Phys 2011;110:33531.
- [28] Bourdin B, Larsen CJ, Richardson CL. A time-discrete model for dynamic fracture based on crack regularization. Int J Fract 2011;168:133–43. <https://doi.org/10.1007/s10707-010-9562-x>.
- [29] Levitas VI, Jafarzadeh H, Farrahi GH, Javanbakht M. Thermodynamically consistent and scale-dependent phase field approach for crack propagation allowing for surface stresses. Int J Plast 2018. <https://doi.org/10.1016/j.ijplas.2018.07.005>.
- [30] Cassenti B, Staroselsky A, Fernando G. A physics-based Lagrangian for the heat-diffusion equation. Philos Mag Lett 2013;93:307–15.
- [31] Roy S, Vasudeva Murthy AS, Kudenatti RB. A numerical method for the hyperbolic-heat conduction equation based on multiple scale technique. Appl Numer Math 2009;59:1419–30.
- [32] Walton AJ. Three phases of matter vol. 530. Oxford: Clarendon Press; 1983.
- [33] Peierls R. The size of a dislocation. Proc Phys Soc 1940;52:34.
- [34] Nabarro FRN. Dislocations in a simple cubic lattice. Proc Phys Soc 1947;59:256.
- [35] Cottrell AH. Theory of crystal dislocations; 1964.

- [36] Cherepanov GP. Mechanics of brittle fracture. New York: McGraw-Hill; 1979.
- [37] Staroselsky A. Damage and cracking morphology. In: Varvani-Farahani A, Brebbia CA, editors. Advances in fracture and damage assessment of materials. UK: WIT Press; 2004.
- [38] Mathioudakis AN. Finite element formulation of phase field fracture. Citeseer 2014.
- [39] Schneider D, Schoof E, Huang Y, Selzer M, Nestler B. Phase-field modeling of crack propagation in multiphase systems. *Comput Methods Appl Mech Eng* 2016;312:186–95.
- [40] Matweb. <http://www.matweb.com/search/datasheet.aspx?MatGUID=2076184469d740af9f86b0d69b2e42ff&ckck=1>; n.d.
- [41] COMSOL M. 3.3: Manual structural mechanics module; 2006. p. 323–346.
- [42] Bowie OL. Rectangular tensile sheet with symmetric edge cracks. *J Appl Mech* 1964;31:208–12.
- [43] Paris PC, Sih GC. Stress analysis of cracks. *Fract. toughness Test. its Appl.* ASTM International; 1965.
- [44] Tweed J, Rooke DP. The distribution of stress near the tip of a radial crack at the edge of a circular hole. *Int J Eng Sci* 1973;11:1185–95.
- [45] Lin S, Hills DA, Nowell D. The solution of cracks emanating from circular holes. *J Strain Anal Eng Des* 1996;31:235–42.
- [46] Lin S, Hills DA. Stress intensity factors for cracks emanating from a semicircular notch in a half-plane. *J Strain Anal Eng Des* 1996;31:433–9.
- [47] Yamamoto Y, Sumi Y, Ao K. Stress intensity factors of cracks emanating from semi-elliptical side notches in plates. *Int J Fract* 1974;10:593–5.
- [48] Hartranft RJ, Sih GC. Alternating method applied to edge and surface crack problems. *Methods Anal. Solut. crack Probl.* Springer; 1973. p. 179–238.
- [49] Pham KH, Ravi-Chandar K, Landis CM. Experimental validation of a phase-field model for fracture. *Int J Fract* 2017;205:83–101.
- [50] Horii H, Nemat-Nasser S. Compression-induced microcrack growth in brittle solids: axial splitting and shear failure. *J Geophys Res Solid Earth* 1985;90:3105–25.
- [51] Arshon IS, Staroselsky AV. Crack development in plane under the action of compressive load. *Sov Appl Mech* 1990;26:878–84.
- [52] Kobayashi M, Shibano J. Bifurcation analysis of fracture mode by simulated and experimental ductile fracture progress based on the proposed crack opening criterion. *Int J Solids Struct* 2018;141:297–315.
- [53] Cueto-Felgueroso L, Juanes R. Stability analysis of a phase-field model of gravity-driven unsaturated flow through porous media. *Phys Rev E* 2009;79:36301.
- [54] Karma A, Lobkovsky AE. Unsteady crack motion and branching in a phase-field model of brittle fracture. *Phys Rev Lett* 2004;92:245510.
- [55] Arriaga M, Waisman H. Multidimensional stability analysis of the phase-field method for fracture with a general degradation function and energy split. *Comput Mech* 2018;61:181–205.
- [56] Cassenti BN. Molecular dynamics and constitutive modeling. *Const. laws Eng. Mater. Recent Adv. Ind. Infrastruct. Appl. Proc. Third Int. Conf. Const. Laws Eng. Mater. Appl.* held January 7–12, 1991, vol. 1. 1991. p. 21.
- [57] Bourdin B, Francfort GA, Marigo J-J. Numerical experiments in revisited brittle fracture. *J Mech Phys Solids* 2000;48:797–826.